 CMES, vol.40, no.3, pp.225-269, 2009

Hypersingular meshless method for solving 3D potential problems with arbitrary domain

D. L. Young[1,3], K. H. Chen[2], T. Y. Liu[3], L. H. Shen[3] and C. S. Wu[3]

Abstract: In this article, a hypersingular meshless method (HMM) is extended to solve 3D potential problems for arbitrary domains after a 2D model was successfully developed (Young et al. 2005a). The solutions are represented by a distribution of the double layer potentials instead of the single layer potentials as generally used in the conventional method of fundamental solutions (MFS). By using the desingularization technique to regularize the singularity and hypersingularity of the double layer potentials, the source points can be located exactly on the real boundary to avoid the sensitivity of locating fictitious boundary for putting the singularity outside the computational domain as usually faced by the conventional MFS. As a result the diagonal terms of influence matrices are easily determined, and the main singular difficulty of the coincidence of the source and collocation points is then overcome. The numerical evidences of the proposed HMM demonstrate the accuracy of solutions after comparing results with analytical solution, conventional MFS, finite element and local differential quadrature methods for the Dirichlet, Neumann and mixed-type boundary conditions of interior problems with simple and complicated domains. Good agreement with analytical solutions and other numerical results is observed.

Keywords: 3D Laplace equations, method of fundamental solutions, mixed-type boundary conditions, hypersingular meshless method, double layer potential, desingularization technique, singularity, hypersingularity, kernel function, circulants theory.

1 Introduction

Recently, scientific researchers have paid much attention to the investigations of the meshless methods. These methods have the characteristics free from mesh and

[1] Corresponding author. E-mail: dlyoung@ntu.edu.tw, Tel and Fax: 886-2-23626114.
[2] Department of Civil Engineering, National I-Lan University, I-Lan, Taiwan.
[3] Department of Civil Engineering and Hydrotech Research Institute, National Taiwan University, Taipei, Taiwan.

element generations. The meshless methods further improve the mesh reduction methods such as the boundary element method (BEM) without necessity to generate grid and mesh and only requiring boundary points. The mesh reduction and meshless techniques possess great potentials to become rivals to the finite volume method (FVM), finite element method (FEM) and finite difference method (FDM) as called the dominant numerical methods. Since there are no requirements of domain or surface meshing, the meshless methods have become very attractive for engineers in model creation, and important tools for scientific computing nowadays.

There are many meshless numerical methods developed recently and among the two most popular schemes at present are the method of fundamental solutions (MFS) and the meshless local Petrov Galerkin (MLPG) methods. The MFS and MLPG have been broadly applied to solve many interesting sciences and engineering problems, such as the potential problems (Fairweather and Karageorghis 1998; Cheng *et al.* 2000; Smyrlis and Karageorghis 2001; Young *et al.* 2002; Tsai *et al*. 2006; Vavourakis *et al*. 2006; Ma 2007; Liu 2008; Ma 2008; Pini *et al*. 2008), elasticity (Shiah *et al*. 2008), fluid mechanics (Tsai *et al*. 2002), heat transfer (Ling and Takeuchi 2008; Hu *et al.* 2008), electromagnetic and acoustic wave propagation (Young and Ruan 2005; Godinho *et al.* 2007; Antonio *et al.* 2007), eigenanalysis (Reutskiy 2004; Alves and Antunes 2005; Chen *et al.* 2005; Young *et al.* 2006a; Reutskiy 2006), biharmonic and polybiharmonic problems (Jin 2004; Tsangaris *et al.* 2004; Tsai 2008), and inverse problems (Hon and Wei 2005; Marin 2008). The MFS and MLPG are both the types of meshless methods, where only boundary points are distributed in the MFS and MLPG (BIE). A comprehensive survey of the MFS was reviewed by Fairweather and Karageorghis (1998) while the MLPG can be referred to Atluri (2004).

The solution procedure makes use of the fundamental solutions, which satisfies the governing equation automatically in the interested domain. To avoid the singularity problem, the solution is represented as a set of singular kernels or the single layer potentials distributed on a non-physical (fictitious) boundary outside the computational domain. The kernel function composes two-point function which is a kind of radial basis functions (RBFs). The independent variables of the two-point function depend only on point position and distance. A regular singularity-free formulation was obtained as a result, and achieving an attractive truly boundary-type and mathematically simple meshfree method. However because of the controversial issue in choosing artificial (fictitious) boundary outside the physical domain, the conventional MFS is still not a very popular numerical method since it has some sensitive problems in locating the fictitious boundary especially for complex geometry and nontrivial boundary conditions (BCs). The meaning of fictitious boundary is an

auxiliary boundary to offset a distance d from the real boundary to avoid the singularities. The distance is generally obtained by the trial and error process or through the judgment of past experiences. For realistic large scale engineering problems especially for complicated geometries and BCs, the fictitious boundary distance is rather difficult to determine since it is not known *a priori*. The diagonal coefficients of influence matrices are divergent due to the point collocation when the fictitious boundary approaches to the real boundary. Despite its gain in singularity free, the influence matrices become ill-posed when the fictitious boundary is too far away from the real boundary. It results in an ill-conditioned problem since the condition numbers for the influence matrices become very large. The location of source and observation points is vital to the accuracy and stability of the solution by implementing the conventional MFS especially for the complex domains and nontrivial BCs.

We have recently carried out a series of research on the HMM to overcome the drawbacks of fictitious boundary in the conventional MFS (Young *et al.* 2005a, 2006b, 2007; Chen *et al.* 2006). The HMM has been successfully used to solve 2D potential (Young *et al.* 2005a; Chen *et al.* 2006; Young *et al.* 2007) and 2D acoustics (Young *et al.* 2006b) problems. Following the fundamental concepts of 2D potential problems (Young *et al.* 2005a), in this paper we further extend the HMM to solve the 3D potential problems based on the potential theory and the desingularization of subtracting and adding-back technique (Tournour and Atalla 1999; Hwang *et al.* 2002; Young *et al.* 2005b). To remove the singularity, it is necessary to regularize the singularity and hypersingularity from the kernel functions. The proposed method is to distribute the observation and source points on the coincident locations of the real boundary. This scheme even uses hypersingular double layer potentials and still preserves the relevant spirits of the MFS. The diagonal terms of the influence matrices can be obtained analytically for spherical domain or numerically for irregular domains by using the proposed technique. The influence coefficients by numerical methods are also compared with analytical derivation by using separable kernels (Abramowitz and Stegun 1972) and circulants theory (Davis 1979) for the special spherical domain. Finally a new algorithm of the HMM is constructed to solve 3D Laplace problems subject to the Dirichlet, Neumann and mixed-type BCs. The continuous or discontinuous BCs with the smoothly and non-smoothly simple and complicated domains are included to illustrate the potentiality and simplicity of the proposed HMM algorithm.

2 Formulation

Consider a boundary value problem with a potential $\phi(x)$, which satisfies the 3D Laplace equation as follows:

$$\nabla_3^2 \phi(x) = 0, \quad x \in D \tag{1}$$

subjected to BCs:

$$\phi(x) = \bar{\phi}, \quad x \in B_1 \tag{2}$$

$$\psi(x) = \bar{\psi}, \quad x \in B_2 \tag{3}$$

where ∇_3^2 is the 3D Laplacian operator, D is the domain of the problem. The BCs are described as follows: where $\psi(x) = \frac{\partial \phi(x)}{\partial n}$, and B_1 is the essential (Dirichlet) boundary in which the potential is prescribed by $\overline{\phi}$, B_2 is the natural (Neumann) boundary in which the normal derivative is prescribed as $\overline{\psi}$; and B_1 and B_2 construct the whole boundary of the domain D as well as the outside domain D^e as shown in Fig. 1 The real physical problems for the Laplace equation contain potential flow problems, steady heat conduction problems, torsion bar problems, Stokes equations of the vorticity transport equations, etc. By employing the RBFs technique [Chen and Tanaka 2002; Young *et al.* 2002; Chen *et al* 2002a; 2002b], the representation of the solutions for interior problems can be approximated in terms of the strengths α^j of the singularities s^j as:

$$\phi(x^i) = \sum_{j=1}^{N} A^{(i)}(s^j, x^i)\alpha^j \tag{4}$$

$$\psi(x^i) = \sum_{j=1}^{N} B^{(i)}(s^j, x^i)\alpha^j, \tag{5}$$

where $A^{(i)}\left(s^j, x^i\right)$ is RBF in which the superscript (i) denotes the interior domain, α^j are the $j-th$ unknown coefficients (strengths of the singularities), s^j is $j-th$ source point (singularity), x^i is $i-th$ observation point, N is the number of source points and $B^{(i)}\left(s^j, x^i\right) = \frac{\partial A^{(i)}\left(s^j, x^i\right)}{\partial n_x}$. After BCs are satisfied by the method of collocation at the boundary points, $\left\{x^i\right\}_{i=1}^N$, the coefficients $\left\{\alpha^j\right\}_{j=1}^N$ can be determined. In Fig. 1 the distributions of source points and observation points are shown for the interior problems. The descriptions of the terminologies of two-point function, fictitious boundary and strength of singularity, observation points, source points, field points, collocation points and boundary points, can also be found from references [Chen *et al.* 2002a; Young *et al*. 2005a; Chen *et al.* 2006].

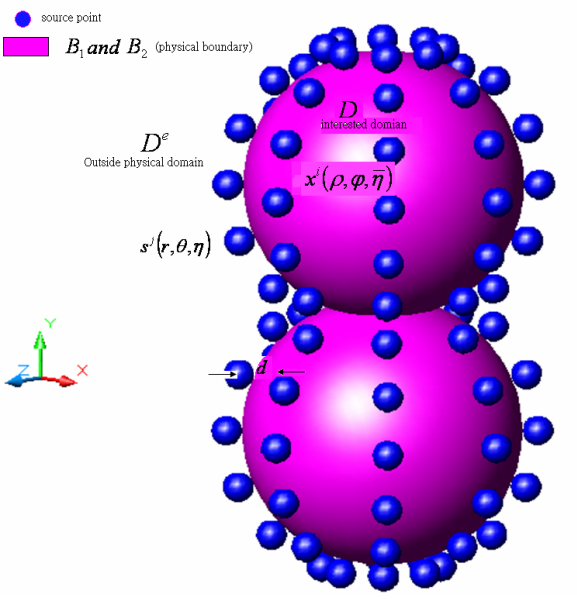

(a)

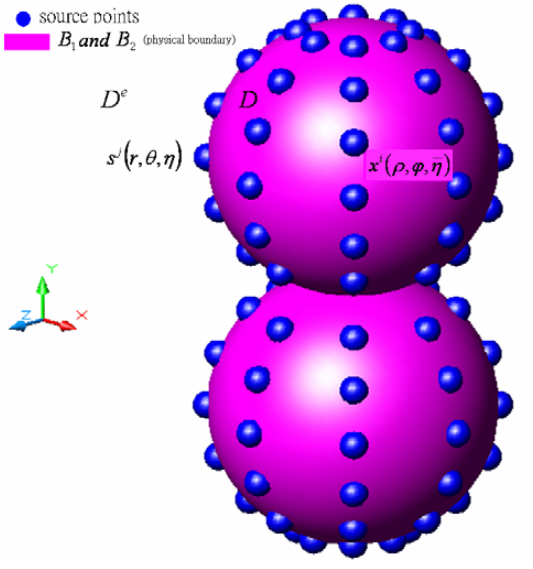

(b)

Figure 1: The source point and observation point distributions and definitions of r, θ, η; ρ, φ, $\overline{\eta}$ for interior problems by using (a) MFS (b) HMM.

By collocating N numbers of observation points to match with the BCs in Eq. (4) for Dirichlet problems and Eq. (5) for the Neumann problems, we have the following linear systems of the form

$$\begin{bmatrix} a_{1,1} & a_{1,2} & \cdots & a_{1,N} \\ a_{2,1} & a_{2,2} & \cdots & a_{2,N} \\ \vdots & \vdots & \ddots & \vdots \\ a_{N,1} & a_{N,2} & \cdots & a_{N,N} \end{bmatrix} \left\{ \alpha^j \right\} = \left[A^{(i)} \right] \left\{ \alpha^j \right\} = \left\{ \overline{\phi}^{(i)} \right\}, \tag{6}$$

$$\begin{bmatrix} b_{1,1} & b_{1,2} & \cdots & b_{1,N} \\ b_{2,1} & b_{2,2} & \cdots & b_{2,N} \\ \vdots & \vdots & \ddots & \vdots \\ b_{N,1} & b_{N,2} & \cdots & b_{N,N} \end{bmatrix} \left\{ \alpha^j \right\} = \left[B^{(i)} \right] \left\{ \alpha^j \right\} = \left\{ \overline{\psi}^{(i)} \right\}, \tag{7}$$

where

$$a_{i,j} = A^{(i)}(s^j, x^i), \quad i, j = 1, 2, \cdots, N \tag{8}$$

$$b_{i,j} = B^{(i)}(s^j, x^i), \quad i, j = 1, 2, \cdots, N \tag{9}$$

A linear combination of Eqs. (6) and (7) can be made to satisfy the mixed-type BCs for the mixed-type problems. After solving the unknown density functions $\left\{ \alpha^j \right\}_{j=1}^{N}$ with the linear algebraic solver, the solutions for the interested domain are calculated from the Eqs. (4) and (5).

The chosen RBF's in this study will be the double layer potentials in the potential theory and are derived in Appendix A for the interior problems or can be found in references [Chen et al. 2002b; 2007] as

$$A^{(i)}\left(s^j, x^i\right) = -\frac{y_k n_k}{\overline{r}_{ij}^3} \tag{10}$$

$$B^{(i)}\left(s^j, x^i\right) = \frac{n_k \overline{n_k} \overline{r_{ij}^2} - 3 y_k y_l n_k \overline{n_l}}{\overline{r}_{ij}^5} \tag{11}$$

where $\overline{r_{ij}} = \left| s^j - x^i \right|$, n_k is the $k-th$ component of the outward normal vector at s^j; $\overline{n_k}$ is the $k-th$ component of the outward normal vector at x^i and $y_k = x_k^i - s_k^j$. The chosen RBF is a kind of the two-point function.

It is noted that the double layer potentials have both singularity and hypersingularity at the origin, which can lead to annoying singular kernels and controversially auxiliary boundary in the conventional MFS. As shown in Fig. 1(a) the off-set distance between the fictitious (auxiliary) boundary (B') and the real boundary (B)

defined by (d), needs to be chosen deliberately. To circumvent the above-mentioned drawback, s^j is distributed on the real boundary as shown in Fig. 1(b) by using the proposed regularization technique. The rationale for choosing double layer potential instead of the single layer potential as used in the proposed method for the form of RBFs, is to take advantage of the desingularization of the subtracting and adding-back technique, so that no off-set distance is needed when evaluating the diagonal coefficients of influence matrices. The single layer potential can not be chosen as the form of RBFs, since Eqs.(14) and (15) in Section 3 are not satisfied by single layers but only by double layers. As a result in case the single layer potential is used, the desingularization of subtracting and adding-back technique fails, and this principle has been proved already (Young *et al.* 2005a; Young *et al*. 2006b).

3 Derivation of diagonal coefficients of influence matrices for arbitrary domain

When the source point s^j approaches to the collocation point x^i, Eqs. (4) and (5) will become singular. Equations (4) and (5) need to be regularized by using special treatment of the desingularization of subtracting and adding-back technique [Young *et al.* 2005a, 2006] as follows:

$$\begin{aligned}\phi\left(x^i\right) &= \sum_{j=1}^{N} A^{(i)}\left(s^j,x^i\right)\alpha^j - \sum_{j=1}^{N} A^{(e)}\left(s^j,x^i\right)\alpha^j \\ &= \sum_{j=1}^{i-1} A^{(i)}\left(s^j,x^i\right)\alpha^j + \sum_{j=i+1}^{N} A^{(i)}\left(s^j,x^i\right)\alpha^j \\ &\quad + \left[\sum_{m=1}^{N} A^{(i)}\left(s^m,x^i\right) - A^{(i)}\left(s^i,x^i\right)\right]\alpha^i, \quad x^i \in B\end{aligned} \tag{12}$$

$$\begin{aligned}\psi\left(x^i\right) &= \sum_{j=1}^{N} B^{(i)}\left(s^j,x^i\right)\alpha^j - \sum_{j=1}^{N} B^{(e)}\left(s^j,x^j\right)\alpha^j \\ &= \sum_{j=1}^{i-1} B^{(i)}\left(s^j,x^i\right)\alpha^j + \sum_{j=i+1}^{N} B^{(i)}\left(s^j,x^i\right)\alpha^j \\ &\quad - \left[\sum_{m=1}^{N} B^{(i)}\left(s^m,x^i\right) - B^{(i)}\left(s^i,x^i\right)\right]\alpha^i, \quad x^i \in B\end{aligned} \tag{13}$$

in which

$$\sum_{j=1}^{N} A^{(i)}(s^j,x^i) = 0, \quad x^i \in B \tag{14}$$

$$\sum_{j=1}^{N} B^{(i)}(s^j, x^i) = 0, \quad x^i \in B. \tag{15}$$

The superscripts (i) and (e) stand for the interior and exterior domains respectively. Detailed derivations of Eqs. (14) and (15) are given in Appendix A. The original singular terms of $A^{(i)}\left(s^i, x^i\right)$ and $B^{(i)}\left(s^i, x^i\right)$ in Eqs. (4) and (5) have been transformed into regular terms

$$\left[\sum_{m=1}^{N} A^{(i)}\left(s^m, x^i\right) - A^{(i)}\left(s^i, x^i\right)\right]$$

and

$$-\left[\sum_{m=1}^{N} B^{(i)}\left(s^m, x^i\right) - B^{(i)}\left(s^i, x^i\right)\right]$$

in Eqs. (12) and (13), respectively. In which the terms of $\sum_{m=1}^{N} A^{(i)}\left(s^m, x^i\right)$ and $\sum_{m=1}^{N} B^{(i)}\left(s^m, x^i\right)$ are the adding-back terms and the terms of $A^{(i)}\left(s^i, x^i\right)$ and $B^{(i)}\left(s^i, x^i\right)$ are the subtracting terms in the two brackets for the special treatment technique. After applying the desingularization of subtracting and adding-back technique (Young *et al*. 2005a), the singularity and hypersingularity of the kernel functions can be removed. Therefore, the diagonal coefficients for the interior problems can be extracted out as:

$$\left\{\phi^i\right\} = \begin{bmatrix} \sum_{m=1}^{N} a_{1,m} - a_{1,1} & a_{1,2} & \cdots & a_{1,N} \\ a_{2,1} & \sum_{m=1}^{N} a_{2,m} - a_{2,2} & \cdots & a_{2,N} \\ \vdots & \vdots & \ddots & \vdots \\ a_{N,1} & a_{N,2} & \cdots & \sum_{m=1}^{N} a_{N,m} - a_{N,N} \end{bmatrix} \left\{\alpha^j\right\}, \tag{16}$$

$$\left\{\psi^i\right\} = \begin{bmatrix} -\left(\sum_{m=1}^{N} b_{1,m} - b_{1,1}\right) & b_{1,2} & \cdots & b_{1,N} \\ b_{2,1} & -\left(\sum_{m=1}^{N} b_{2,m} - b_{2,2}\right) & \cdots & b_{2,N} \\ \vdots & \vdots & \ddots & \vdots \\ b_{N,1} & b_{N,2} & \cdots & -\left(\sum_{m=1}^{N} b_{N,m} - b_{N,N}\right) \end{bmatrix} \left\{\alpha^j\right\}.$$

(17)

The diagonal terms of the two influence matrices for both interior and exterior problems can also be derived analytically for a special case of spherical domain shown in the Appendix B. The derivation of diagonal terms in the influence matrices of the spherical problem is analyzed by the separable kernel (Abramowitz and Stegun 1972) and circulants theory (Davis 1979). Table 1 shows the properties of the influence matrices for both spherical and arbitrary domains.

4 Numerical results and discussions

To demonstrate the accuracy and validity of the proposed method, the potential problems with spherical, cubic, cylindrical and arbitrary shapes subject to different Dirichlet, Neumann, and mixed-type BCs with continuous and discontinuous BCs are considered in the following examples.

Example 1: Spherical shape case (case 1)

The interior Dirichlet problem with continuous BCs of the spherical domain is taken as the first example. This simply-connected problem with spherical geometry is used to demonstrate the analytic derivation of diagonal terms in the influence matrices as derived in Appendix B. Two numerical methods, the MFS and proposed HMM, are used to compare the accuracy and stability with the analytical solution using the same degrees of freedom. The following case uses 1866 collocating boundary points.

Case 1: Dirichlet problem

Problem sketch and the 1866 nodes distribution with outward normal vectors employing the proposed HMM are depicted respectively in Figs. 2(a) and 2(b). The problem is subjected to Dirichlet continuous BCs as follows:

$$\phi = 1 - \cos 2\eta, \quad \eta : \text{ the solid angle.} \tag{18}$$

In this case, the analytical solution is found to be:

$$\phi = \frac{4}{3} P_0(\cos\eta) - \frac{4}{3} r^2 P_2(\cos\eta), \quad P_n : \text{ Fourier Legendre polynomial.} \tag{19}$$

By using the MFS and distributing the 1866 source points on the fictitious boundary with d=0.5 off-set distance, we obtain the good results of the field potential. It is facile to find out an optimal off-set distance (d) for the spherical shape due to the very simple geometry. The comparisons of numerical results between the analytical

Table 1: The comparison of numerical results and analytical solutions for case 1.

	Results at (y=0, z=0) and x=					RMSE
	x=0.085	x=0.34	x=0.595	x=0.68	x=0.85	
MFS (n=1866)	0.66185	0.58960	0.43065	0.35840	0.18500	7.58E-04
HMM (n=1866)	0.67699	0.60202	0.43669	0.36141	0.18043	1.03E-02
Analytical	0.66185	0.58960	0.43065	0.35840	0.18500	-

(n denotes computational nodes)

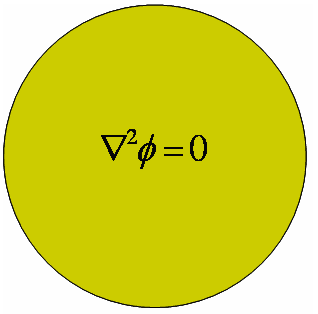

(a) Problem sketch

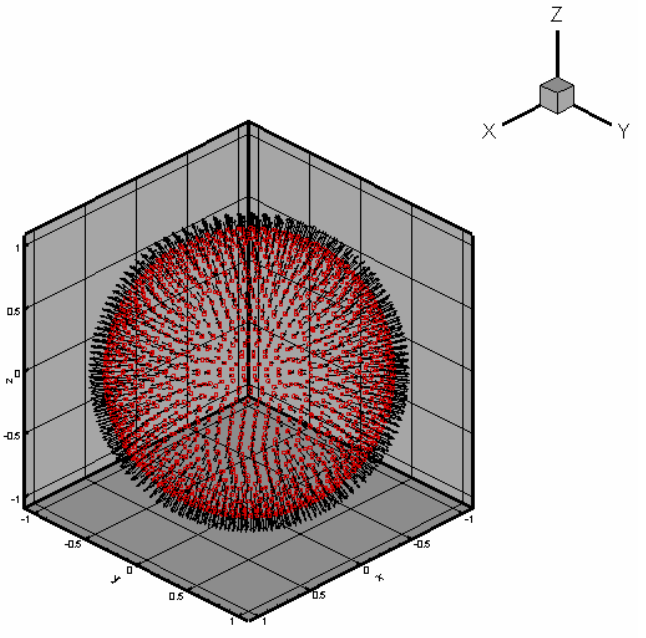

(b) Nodes distribution with normal vectors

Figure 2: (a) Problem sketch and (b) nodes distribution with normal vectors (1866 nodes) for case 1.

solutions at (y=0, z=0) line by using the MFS (d=0.5) and proposed HMM are displayed in Tab. 1. The results of two meshless methods show good agreement with analytical solutions. However as expected the MFS with a RMSE 7.58E-4 will give a better solution than the HMM with a RMSE 1.03E-2 due to an optimal

off-set distance is found in the MFS, since the MFS adopts single layer potential while the HMM has to use double layer potential. Here the root mean square error (RMSE) is defined as $\sqrt{\frac{\sum_{i=1}^{N}\left|\phi_{analytical}-\phi_{numerical}\right|^2}{N}}$.

Example 2: Cubic shape cases (cases 2-1 and 2-2)

The interior Dirichlet problems with discontinuous BCs are given in cases 2-1 and 2-2. The interior Dirichlet problem is considered in case 2-1, while case 2-2 is devoted to the interior Dirichlet, Neumann mixed-type boundary problem. Both two cases use 1350 boundary nodes.

Case 2-1: Dirichlet problem

Problem sketch and the nodes distribution with outward normal vectors employing the proposed HMM are depicted in Figs. 3(a) and 3(b) respectively. The problem is subjected to the following Dirichlet discontinuous BCs:

$$\phi(x,y,1)=1, \quad \phi(x,y,0)=\phi(x,0,z)=\phi(x,1,z)=\phi(0,y,z)=\phi(1,y,z)=0 \quad (20)$$

In this case, an analytical solution is found as follows:

$$\phi=\sum_{m=1}^{\infty}\sum_{n=1}^{\infty}4\sin(m\pi x)\sin(n\pi y)\left[\frac{1-(-1)^m}{m\pi}\right]\left[\frac{1-(-1)^n}{n\pi}\right]\frac{\sinh\left(\sqrt{m^2+n^2}\pi z\right)}{\sinh\left(\sqrt{m^2+n^2}\pi\right)} \quad (21)$$

We obtain the field potential solutions with a RMSE 6.26E-5 using the MFS by distributing 1350 source points on the fictitious boundary with an off-set distance (d=0.5). The ideal off-set distance is easily obtained for this simple cubic shape too. The numerical results using the HMM with 1350 nodes will end up with a RMSE 2.01E-3. If the FEM with 13720 elements and 3375 nodes is adopted we will get a RMSE 4.10E-3. The comparisons of numerical values at (x=0.5, y=0.5) and (x=0.5, z=0.5) lines between the analytical solution by using the proposed HMM, MFS, and the FEM are listed in Tab.2. The results obtained using the present HMM match the analytical solutions very well. To see the error distribution pattern of the cross-section at x=0.5, the absolute error with analytical solution in the interested field with 225 inner points is given in Fig. 4. The large error occurs on the singular corner and the boundary due to the boundary layer effects of the HMM and MFS. The absolute error is defined as $|\phi_{exact}-\phi_{numerical}|$. Among the three numerical schemes we can see that MFS again gives the best accuracy, HMM is the second and FEM is the worst one.

Case 2-2 Dirichlet and Neumann mixed-type problem

Table 2: The comparison of numerical results and analytical solutions for case 2-1.

	Results at (x=0.5, y=0.5) and z=							(n)
	0.07143	0.21429	0.35714	0.5	0.64286	0.78571	0.92857	
MFS	0.01223	0.04163	0.08755	0.16667	0.30276	0.52144	0.82717	1350
FEM	0.01225	0.04164	0.08742	0.16608	0.30122	0.51895	0.82568	3375
HMM	0.01194	0.04162	0.08762	0.16686	0.30306	0.52165	0.83309	1350
Analytical	0.01223	0.04162	0.08755	0.16667	0.30276	0.52144	0.82716	-
(n denotes computational nodes)								
	Results at (x=0.5, z=0.5) and y=							RMSE
	0.07143	0.21429	0.35714	0.5	0.64286	0.78571	0.92857	
MFS	0.04015	0.10923	0.15242	0.16667	0.15242	0.10923	0.04015	6.26E-05
FEM	0.04019	0.1091	0.15197	0.16608	0.15197	0.1091	0.04019	4.10E-03
HMM	0.03943	0.10942	0.15262	0.16686	0.15262	0.10942	0.03943	2.01E-03
Analytical	0.04015	0.10923	0.15242	0.16667	0.15242	0.10923	0.04015	-

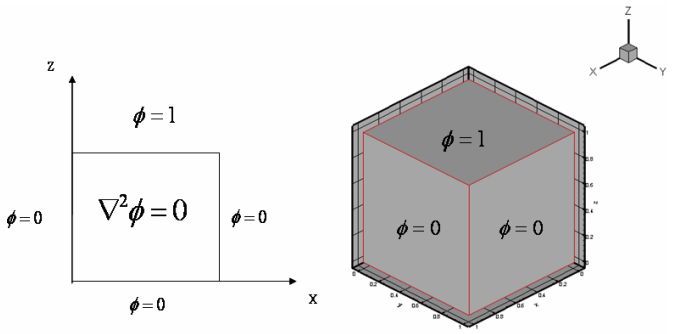

(a) Problem sketch

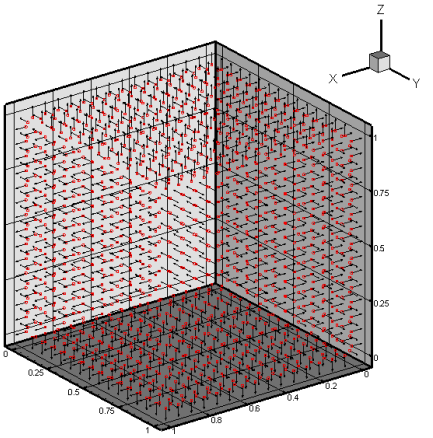

(b) Nodes distribution with normal vectors

Figure 3: (a) Problem sketch and (b) nodes distribution with normal vectors (1350 nodes) for case 2-1.

In this case, we investigate a domain with the Neumann discontinuous BCs at the bottom of the cubic as given below:

$$\phi(x,y,1)=1, \quad \frac{\partial\phi(x,y,0)}{\partial n}=0, \quad \phi(x,0,z)=\phi(x,1,z)=\phi(0,y,z)=\phi(1,y,z)=0 \tag{22}$$

Problem sketch using the proposed HMM is similar to Fig. 4. In this case, an

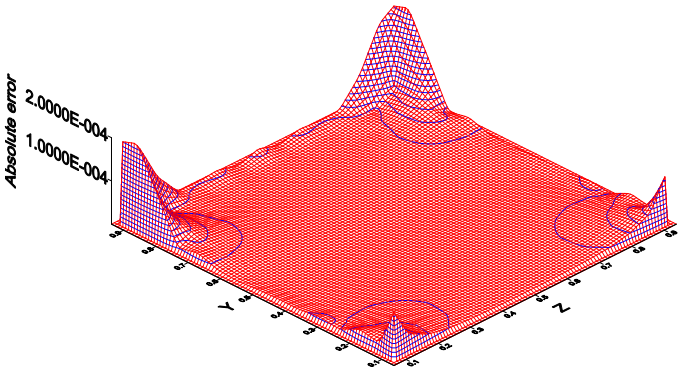

(a) MFS

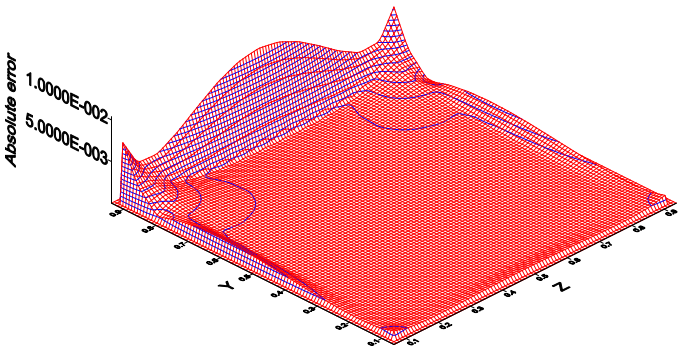

(b) HMM

Figure 4: The error distribution map of cross-section at x=0.5 by using (a) MFS (b) HMM for case 2-1.

analytical solution is available as follows:

$$\phi = \sum_{m=1}^{\infty}\sum_{n=1}^{\infty} 4\sin(m\pi x)\sin(n\pi y)\left[\frac{1-(-1)^m}{m\pi}\right]\left[\frac{1-(-1)^n}{n\pi}\right]\frac{\cosh\left(\sqrt{m^2+n^2}\pi z\right)}{\cosh\left(\sqrt{m^2+n^2}\pi\right)} \tag{23}$$

The field results find that the present HMM with 1350 nodes yields a RMSE 2.02E-3, the conventional MFS (d=0.5) with 1350 nodes reaches a RMSE 8.23E-5 and the FEM with 13720 elements and 3375 nodes will have a RMSE 4.10E-3. The com-

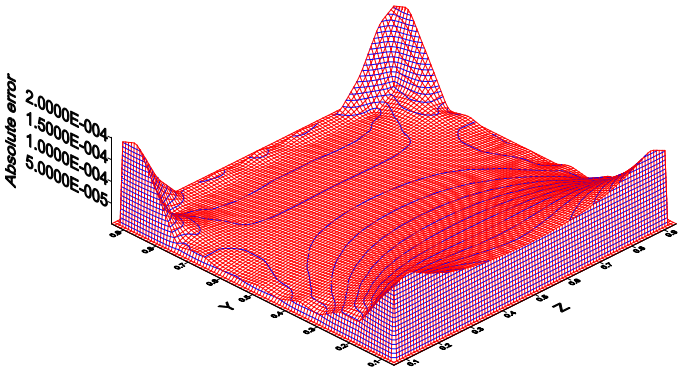

(a) MFS

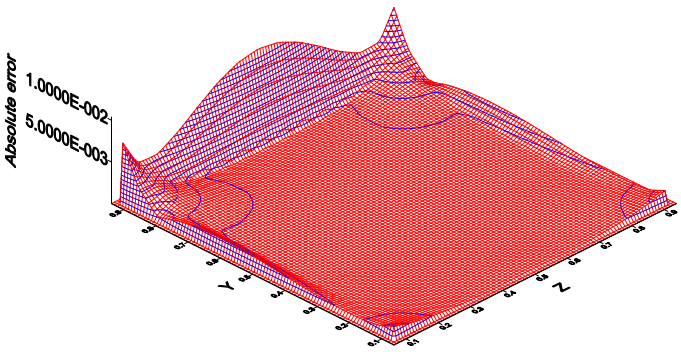

(b) HMM

Figure 5: The error distribution map at x=0.5 cross-section by using (a) MFS (b) HMM for case 2-2.

parison of analytical solutions at (x=0.5, y=0.5) and (x=0.5, z=0.5) lines by using the HMM, MFS and the FEM are shown in Tab.3. In Fig. 5 the error distribution pattern of the interested domain is plotted. The numerical results by using all the methods are very close to the analytical solutions. However the MFS is still a little better than the HMM and FEM, while the HMM is even accurate than the FEM though coarse points are used in the HMM as expected.

Example 3: Cylinder shape case (case 3)

In case 3 the interior Dirichlet problem of cylindrical shape with discontinuous BCs is considered.

Table 3: The comparison of numerical results and analytical solutions for case 2-2.

	Results at (x=0.5, y=0.5) and z=							(n)
	0.07143	0.21429	0.35714	0.5	0.64286	0.78571	0.92857	
MFS	0.03993	0.05632	0.09532	0.17075	0.30487	0.52243	0.82745	1350
FEM	0.04013	0.05646	0.09528	0.17022	0.30335	0.51996	0.82597	3375
HMM	0.04012	0.05633	0.09535	0.17091	0.30514	0.52263	0.83337	1350
Analytical	0.03994	0.05632	0.09532	0.17075	0.30486	0.52243	0.82744	-
(n denotes computational nodes)								
	Results at (x=0.5, z=0.5) and y=							RMSE
	0.07143	0.21429	0.35714	0.5	0.64286	0.78571	0.92857	
MFS	0.04106	0.11177	0.1561	0.17075	0.1562	0.11178	0.04106	8.23E-05
FEM	0.04111	0.11168	0.1557	0.17022	0.1557	0.11168	0.04111	4.10E-03
HMM	0.04031	0.11194	0.15626	0.17091	0.15626	0.11194	0.04031	2.02E-03
Analytical	0.04106	0.11178	0.1561	0.17075	0.1561	0.11178	0.04106	-

Case 3: Interior Dirichlet problem (discontinuous BCs)

A cylinder subjected to the following Dirichlet BCs is considered:

$$\phi(r,\theta,1)=1, \quad \phi(r,\theta,0)=\phi(1,\theta,z)=0. \tag{24}$$

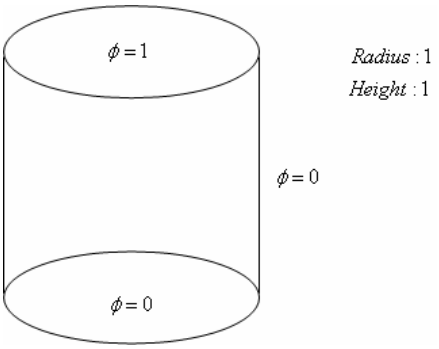

(a) Problem sketch

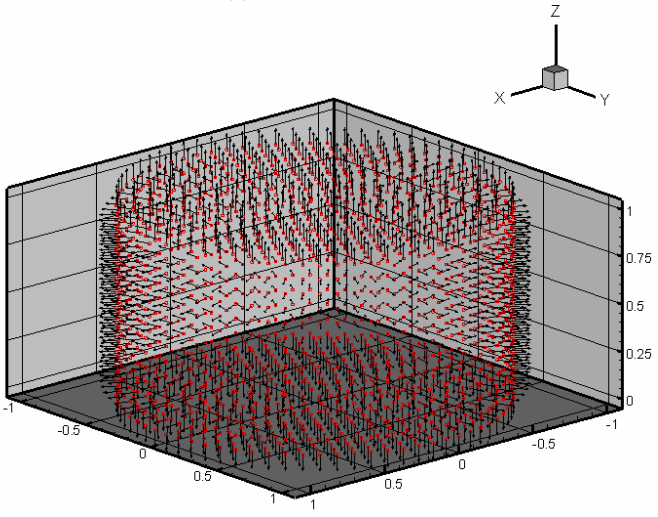

(b) Nodes distribution with normal vectors

Figure 6: (a) Problem sketch and (b) nodes distribution with normal vectors (1800 nodes) for case 3.

Problem sketch and 1800 nodes distributions with outward normal vectors using the proposed HMM are respectively depicted in Fig. 6(a) and 6(b). An analytical

solution is available as follows:

$$\phi = \sum_{n=1}^{\infty} \frac{2}{e^{\alpha_n} - e^{-\alpha_n}} \frac{1}{\alpha_n J_1(\alpha_n)} \left(e^{\alpha_n z} - e^{-\alpha_n z}\right) J_0(\alpha_n r) \tag{25}$$

where

$$\alpha_n : \text{ The } n-th \text{ root of } J_0 \tag{26}$$

We obtain the results by using the MFS for the off-set distance (d) same as case 1. We are able to obtain good results using this distance by numerical experiment. The field solutions with 1800 nodes by the proposed HMM and MFS (d=0.5) reached the accuracy of RMSE 2.84E-2 for HMM, and a RMSE 3.80E-3 for the MFS respectively. Moreover, both results at (x=0,y=0) line are compared with analytical solutions as shown in Tab.4. However the MFS still outperforms the HMM, because an optimal off-set distance of the MFS could be found. In Fig. 7 the error distribution pattern of the interested domain is plotted. For the cylindrical shape, the node distribution severely affects the accuracy when applying the HMM. The comparison of numerical accuracy for the different nodes distributions is shown in Fig. 8. If the nodes are uniformly distributed at the top and bottom circular surfaces of the cylinder as Fig.8 (a) we will get a good RMSE: 2.41E-2. If every circle has the same number of nodes as Fig.8 (b) it ends up with a poor RMSE: 0.1523. If we fix the number of nodes at outside part and increase the number of nodes at inside part in the cylinder as Fig.8 (c) it results in a good RMSE: 8.89E-2. However if we control the number of inside part and outside part separately like Fig. 8 (d) we will have a poor RMSE: 0.1738 again. By applying the mean distance of the nodes from Tab. 5, we know the fact that the most uniform point distribution will provide the best result judging from Fig. 8. Thus the ideal number of nodes on the z-axis can be determined and the best result of the whole computational domain is obtained as shown in Fig. 9. This figure reveals a significant message that uniform convergence and numerical stability are always expected with increasing collocating points in the HMM which is quite different from the MFS. We will encounter a stability problem when the collocation points are too big in the MFS. Moreover the convergence is an exponential function so only very coarse collocating points are required to obtain an optimal solution by the HMM. Occasionally in case when a more dense mesh is needed locally due to the nature of simulating a physical problem, we suggest employing the localization concepts such as domain decomposition techniques (Chen *et al*. 2005) or matrix decomposition algorithm (Tsangaris *et al*. 2004) to tackle the problem. It is certainly a follow-up topic which is worth studying deeply.

Table 4: The comparison of numerical results and analytical solutions for case 3.

	Results at (x=0, y=0) and z=							(n)
	0.08333	0.25	0.41667	0.58333	0.75	0.83333	0.91667	
MFS	0.0552	0.1718	0.30695	0.47005	0.66467	0.77238	0.88501	1800
HMM	0.07004	0.18071	0.32718	0.50156	0.69986	0.79497	0.86072	1800
Analytical	0.05499	0.17139	0.30633	0.46935	0.66408	0.77193	0.88457	-
(n denotes computational nodes)								
	Results at (x=0, z=0.5) and y=							RMSE
	-0.92308	-0.61538	-0.30769	0	0.30769	0.61538	0.92308	
MFS	0.05635	0.2551	0.35642	0.3846	0.35642	0.2551	0.05635	3.80E-03
HMM	0.06406	0.28196	0.38401	0.41078	0.38401	0.28196	0.06406	2.84E-02
Analytical	0.05609	0.25395	0.35559	0.38391	0.35559	0.25395	0.05609	-

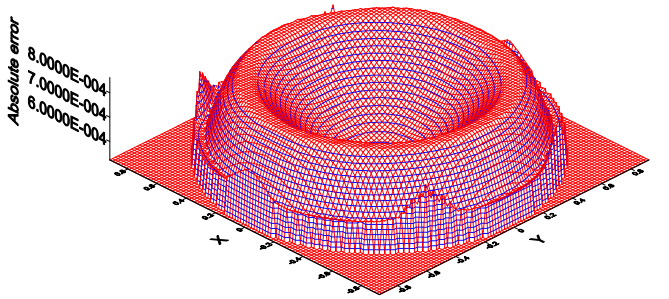

(a) MFS

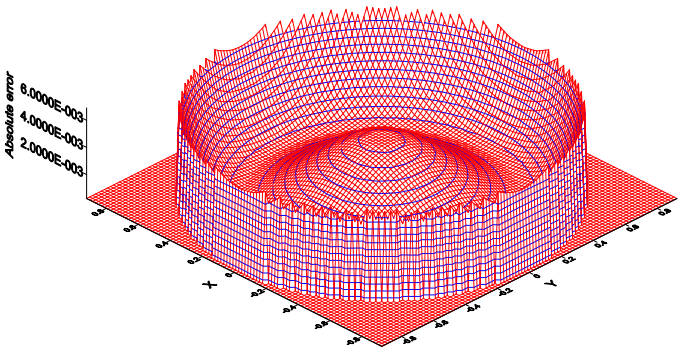

(a) HMM

Figure 7: The error distribution map at z=0.5 cross-section by using (a) MFS (b) HMM for case 3.

Example 4: Ring shape case (case 4)

In case 4 we consider the ring shape of interior Dirichlet problems with discontinuous BCs.

Case 4: Interior Dirichlet problem (discontinuous BCs)

Figs. 10(a) and 10(b) respectively depict problem sketch and 1236 nodes distribution with outward normal vectors using the proposed HMM. A ring shape subjected to the following Dirichlet BCs is considered:

$$\phi(1,\theta,z) = 1, \quad \text{others: } \phi = 0. \tag{27}$$

Hereby we use the MFS and FEM to check the accuracy of the proposed model HMM. Comparison of these three numerical methods at (y=0, z=0.5) and (x=0,

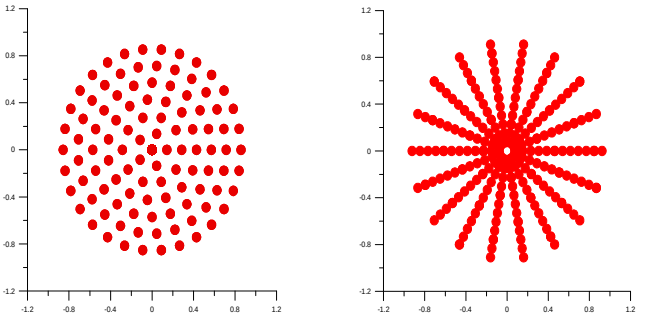

RMSE: 2.41E-2

(a)

RMSE: 0.1523

(b)

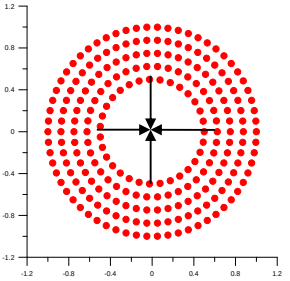

RMSE: 8.89E-2

(c)

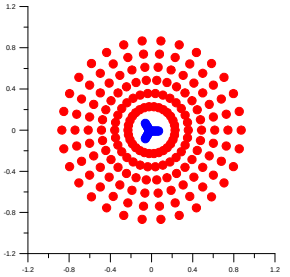

RMSE: 0.1738

(d)

Figure 8: The point distribution of (a), (b), (c), (d) arrangements by using HMM at top and bottom surfaces for case 3.

Table 5: Sensitivity test of point distribution for case 3.

Number of nodes on Z axis	Distance of the nodes on Z axis	RMSE
6	0.1666	0.3764
7	0.1428	0.2871
8	0.1250	0.2131
9	0.1111	0.1510
10	0.1000	9.84E-2
11	0.0909	5.44E-2
12	0.0833	2.41E-2
13	0.0769	3.39E-2
14	0.0714	6.10E-2
15	0.0666	8.73E-2

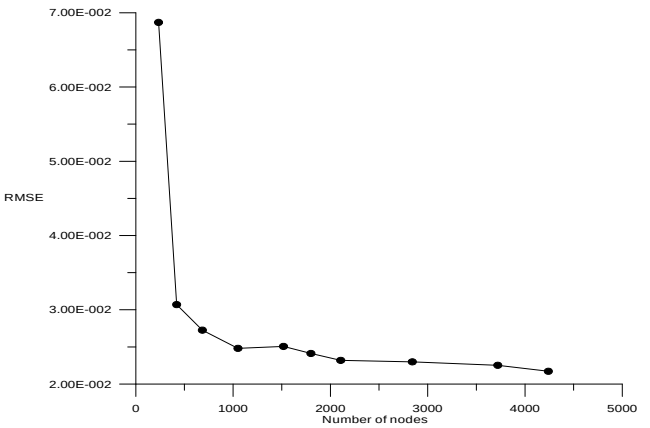

Figure 9: Convergence test of number of the nodes.

z=0.5) lines is presented in Tab.6; it is found that almost the same results are obtained. However there are 5000 elements and 1320 nodes employed in the FEM and only 1236 nodes are used in the HMM and MFS to reach the same accuracy.

Example 5: Dual sphere shape cases (cases 5-1 to 5-3)

In the cases 5-1 to 5-3, the interior Dirichlet problems for the dual sphere shape with continuous and discontinuous BCs are considered.

Case 5-1: Interior Dirichlet problem (trivial continuous BCs)

Problem sketch and 2826 nodes distribution with outward normal vectors are depicted in Figs. 11(a) and 11(b) respectively for more complex linear BCs: $\phi = e^x.\cos y + z$. Analytical solutions $\phi = e^x.\cos y + z$ (using 2826 points to plot the contours) for the considered problem are also shown in Fig. 12. After distributing 2826 nodes, we obtain very unreasonable results by using the MFS for different types and distances of fictitious boundary (d) as depicted in Fig. 13(a) for an intersectional fictitious boundary. Figure 13(b) displays MFS wrong results for d=0.5. It is obvious that the field solutions of the MFS depend not only on the circular fictitious boundary as shown in Fig. 14(a) but also on the offset distance d=0.5 (wrong answer) as shown in Fig. 14(b), and d=1 (correct) with a RMSE 1.26E-4 as shown in Fig.14(c). It is very shocked to observe from Figs. 13(b), 14(b) and 14(c) that the MFS will give correct or wrong solutions depending on the source locations outside the computational domain even the same 2826 source points are adopted. This illustrates an important fact that the location of source points is very crucial to the accuracy of the solution by using the conventional MFS if there is no exact solution available or not first using the HMM solution to serve as guidance.

Table 6: The comparison of numerical results and exact solutions for case 4.

	Results at (y=0, z=0.5) and x=								
	1.11111	1.22222	1.33333	1.44444	1.55556	1.66667	1.77778	1.88889	(n)
MFS	0.71958	0.51524	0.36045	0.24743	0.16610	0.10722	0.06346	0.02917	1236
FEM	0.72418	0.51393	0.35719	0.24247	0.16153	0.10460	0.06253	0.02869	1320
HMM	0.75453	0.50415	0.34844	0.23644	0.15681	0.09985	0.05797	0.02443	1236
(n denotes computational nodes)									
	Results at (x=0, z=0.5) and y=								
	1.11111	1.22222	1.33333	1.44444	1.55556	1.66667	1.77778	1.88889	
MFS	0.71864	0.51519	0.36044	0.24742	0.16609	0.10722	0.06345	0.02917	
FEM	0.72337	0.51389	0.35719	0.24247	0.16154	0.10460	0.06253	0.02875	
HMM	0.75455	0.50418	0.34847	0.23646	0.15683	0.09985	0.05798	0.02510	

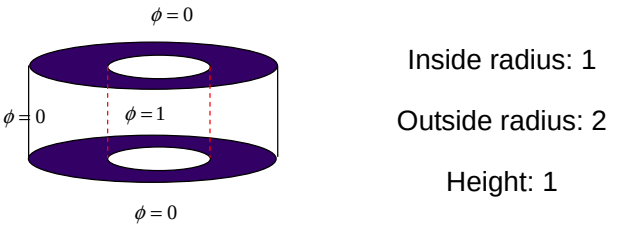

(a) Problem sketch

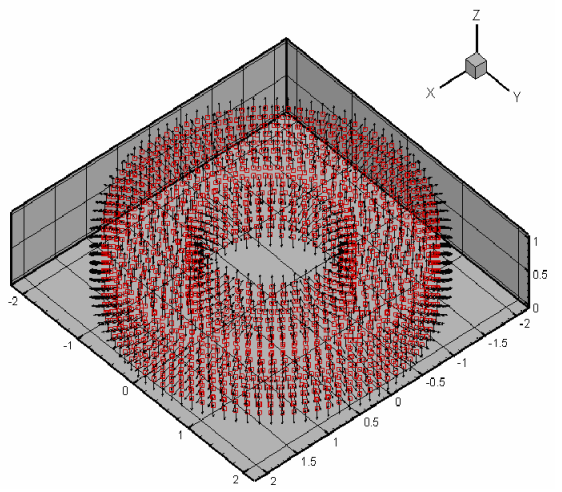

(b) Nodes distribution with normal vectors

Figure 10: (a) Problem sketch and (b) nodes distribution with normal vectors (1236 nodes) for case 4.

In such a situation, the MFS can not yield reliable and consistent solutions if a reasonable off-set distance can not be determined even for this trivial BCs case. Thus the confusion of selecting a meaningful off-set distance in the MFS is avoided by adopting the present HMM. In Fig. 15 the field solutions with a MRSE 4.12E-2 of the proposed HMM show very close results to the analytical solutions.

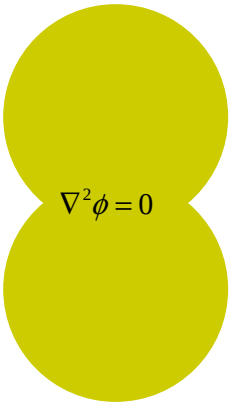

BC: $\phi = e^x \cdot \cos y + z$

(a) Problem sketch

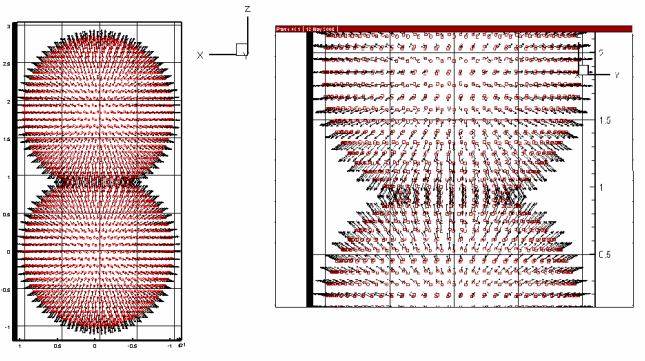

(a) Nodes distribution with normal vectors

Figure 11: (a) Problem sketch (b) nodes distribution with normal vectors (2826 nodes) for case 5-1.

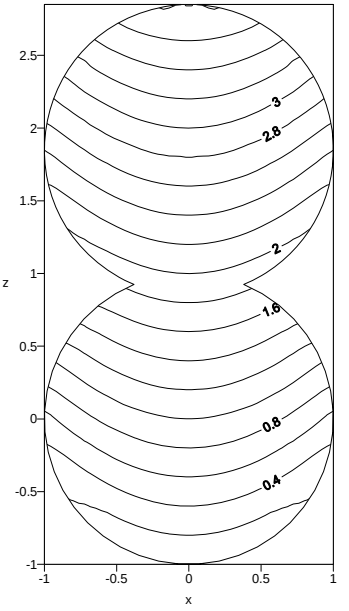

Analytical solution

Figure 12: The analytical solution for case 5-1.

Case 5-2, 5-3: Interior Dirichlet problem (nontrivial BCs)

Problem sketches using the proposed HMM are similar to Fig. 11 for case 5-2 with BCs: $\phi = 1 - \cos 2\eta$; and for case 5-3 with BCs: $\phi = 1$ for upper sphere and $\phi = 0$ for lower sphere. For these nontrivial BCs, it is difficult to find an ideal off-set distance to obtain good results for Case 5-2 and Case 5-3 by the MFS with 2826 nodes and d=1 (wrong answers) as shown respectively in Figs. 16(a) and 17(a). (It will be recalled that for d=1 the MFS will give excellent results for the trivial BCs of Case 5-1 but wrong solutions of nontrivial BCs of Case 5-2 and Case 5-3). Since the cases with the feature of geometric singularity posses no analytical solutions, we use a high order accuracy method, the local differential method (LDQ) (Zong and Lam, 2002) to verify the HMM results. Shen et al. (2007; 2009) further developed the improvement of LDQ method for irregular domains. The results with 2981 nodes are obtained by referring 5 nearest local points along 3 Cartesian axes as in Figs. 16(b) and 17(b), respectively. The proposed HMM with 2826 nodes provides promising results without adjusting any off-set distance as shown respectively in Figs. 16(c) and 17(c). Furthermore, the HMM has solved the problems without any mesh and more efficient than the LDQ. It is important to point out that the selection of appropriate off-set distance of the MFS not only depends on the geometry but

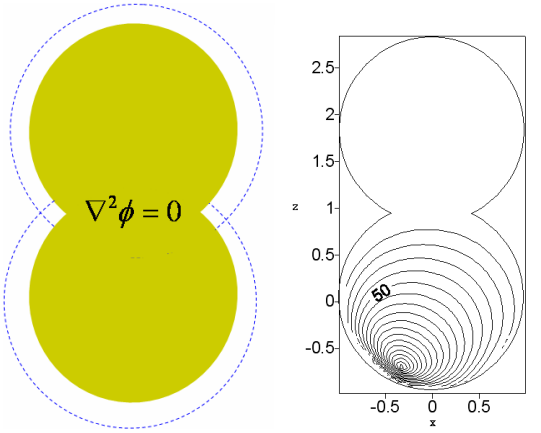

(-------- Fictitious boundary) 2826 nodes
(a) Intersectional fictitious boundary (b) MFS (d=0.5)

Figure 13: (a) Intersectional fictitious boundary location (b) field solutions at z=0 cross-section by using MFS (d=0.5) for case 5-1.

also heavily on the BCs such as demonstrating in cases 5-1 to 5-3 and the following cases 6-1 to 6-3.

Example 6: Pole shape cases (cases 6-1 to 6-3)

In cases 6-1 to 6-3, the interior Dirichlet problems for the pole shape with continuous and discontinuous BCs are given, respectively.

Case 6-1: Interior Dirichlet problem (trivial continuous BCs)

Problem sketch and 2261 nodes distribution with outward normal vectors using the proposed method are depicted in Figs. 18(a) and 18(b), respectively for more complex geometry. Analytical solution for the chosen problem is also shown in Fig. 19. After distributing 2261 nodes, we obtain the results by using the MFS, with circular fictitious boundary, for different off-set distances (d) as depicted in Fig. 20. It is obvious to observe that the field solutions of the MFS with d=2 (wrong answer) by experience judgment, is worse than d=1.2 (correct answer) with RMSE 1.34E-4, by adjusting to match the analytical solution as shown in Fig. 20(a) and Fig. 20(b) respectively. This demonstrates how sensitive for a reliable solution obtained by MFS from observing a very marginal range of the off-set distance chosen from the boundary. In Fig. 20(c) the field solutions of the proposed HMM with a RMSE 4.11E-2 reveal good result as comparing with analytical solutions.

Cases 6-2, 6-3: Interior Dirichlet problems (nontrivial BCs)

Problem sketch using the proposed method are similar to Fig. 18 for case 6-2 with

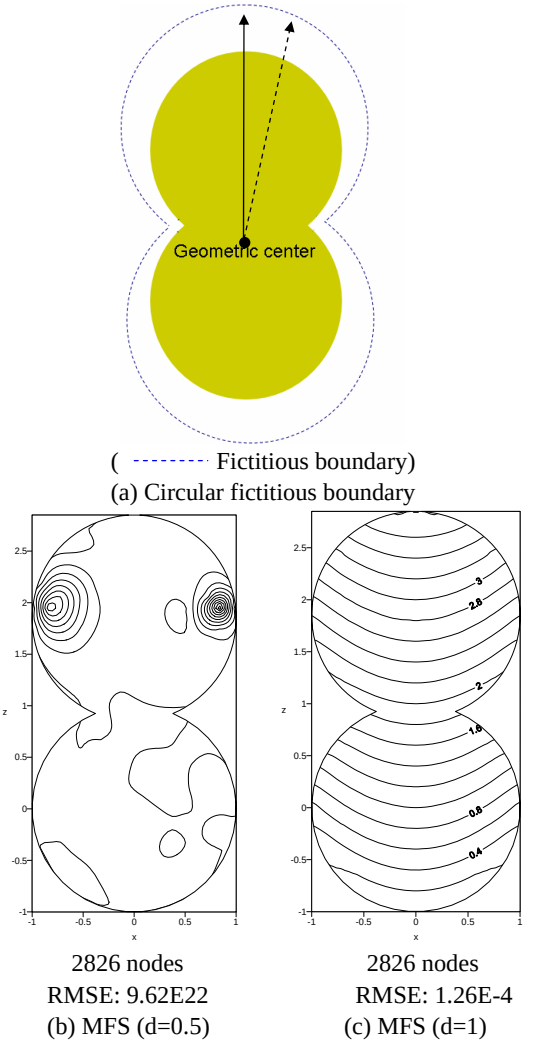

Figure 14: (a) Circular fictitious boundary location and field solutions at z=0 cross-section by using (b) MFS (d=0.5) and (c) MFS (d=1) for case 5-1.

BCs: $\phi = 1$ for upper sphere and $\phi = 0$ for lower cylinder; and for case 6-3 with BCs: $\phi = 1 - \cos 2\eta$ for upper sphere and $\phi = 0$ for lower cylinder. For these nontrivial BCs, it is still difficult to find ideal offset distance to obtain good results for nontrivial BCs of Case 6-2 and Case 6-3 by using MFS with 2261 nodes and d=1.2 (wrong answers) as shown in Figs. 21(a) and 22(a), respectively. The MFS for modeling Case 6-2 and Case 6-3 draws almost the similar conclusion as Case

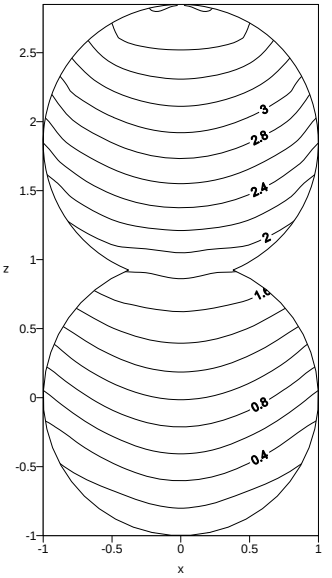

2826 nodes
RMSE: 4.12E-2
HMM

Figure 15: The field solutions at y=0 cross-section by using HMM for case 5-1.

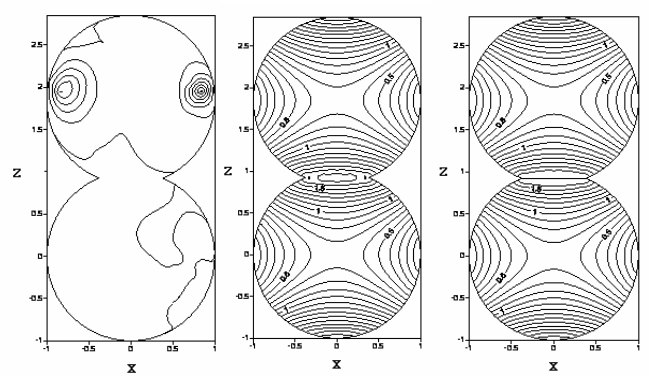

2826 nodes (a) MFS (d=1) | 2981 nodes (b) LDQ | 2826 nodes (c) HMM

Figure 16: The field solutions at z=0 cross-section by using (a) MFS (d=1) (b) LDQ (c) HMM for case 5-2.

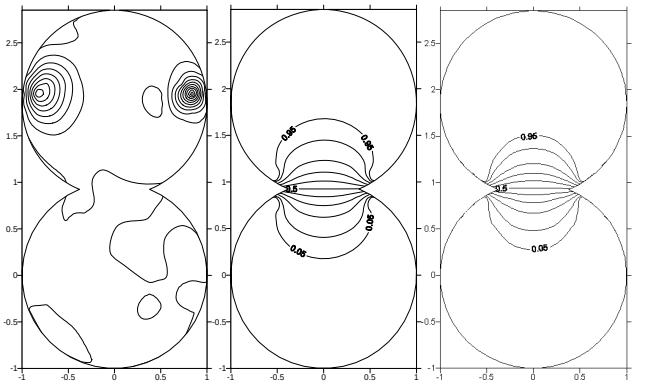

2826 nodes (a) MFS (d=1) | 2981 nodes (b) LDQ | 2826 nodes (c) HMM

Figure 17: The field solutions at z=0 cross-section by using (a) MFS (d=1) (b) LDQ (c) HMM for case 5-3.

5-2 and Case 5-3. It is recalled that for d=1.2 the MFS will give excellent results for the trivial BCs of Case 6-1 but wrong solutions of nontrivial BCs of Case 6-2 and Case 6-3. The results of the LDQ with 2310 nodes are obtained by referring 5 nearest local points along three Cartesian axes as depicted in Figs. 21(b) and 22(b), respectively. The proposed HMM with 2261 nodes still provides good solutions in comparing with the LDQ results as shown respectively in Figs. 21(c) and 22(c).In these two cases we are not able to get meaningful solutions by the conventional MFS unless HMM or LQD is employed.

5 Conclusions

In this article we implement the HMM to solve the 3D Laplace problems for arbitrary domains subject to the Dirichlet, Neumann and mixed-type BCs. Only the boundary nodes on the real boundary are required. The major difficulty of the coincidence of the source and collocation points in the conventional MFS is then circumvented. Moreover the controversy of the artificial (fictitious) boundary outside the physical domain by using the MFS no longer exists. From the present study for irregular domains with nontrivial BCs, the conventional MFS has to spend a lot of efforts to search for the optimal off-set distance for each assigned number of source points. There is possible we will face with difficulty to find a meaningful solution. On the other hand, an acceptable answer with logarithmic convergence always can be easily obtained by using the HMM. Furthermore from the sensitivity analysis of point distribution and seeding it is found that the HMM requires uniform point

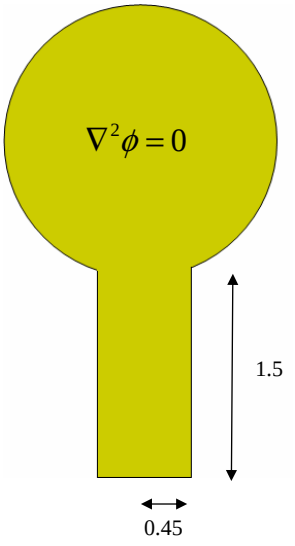

BC: $e^y \cdot \sin z + x$

(a) Problem sketch

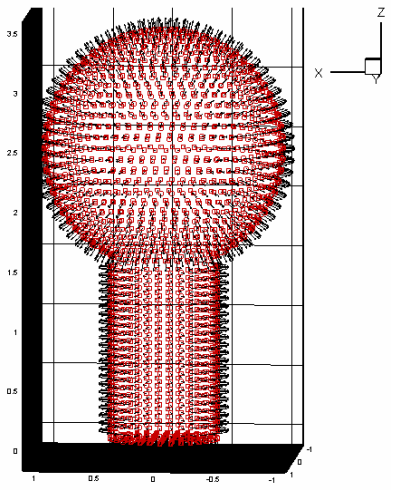

(b) Nodes distribution with normal vectors

Figure 18: (a) Problem sketch (b) nodes distribution with normal vectors (2261 nodes)

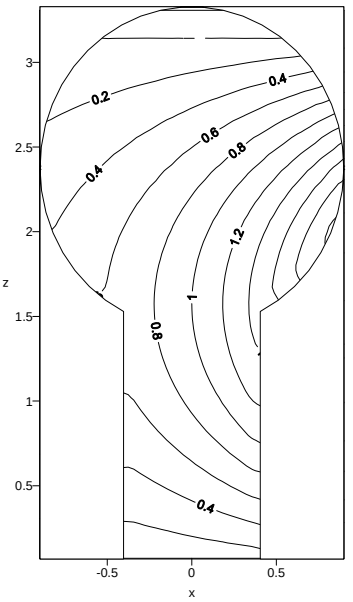

Figure 19: Analytical solution for case 6-1.

distribution to obtain a better accuracy. The numerical results were obtained by using the developed program for six category examples with different BCs and domain shapes. Solutions were compared very well with the analytical solutions or other numerical methods such as the FEM, LDQ and MFS especially for irregular domains and the nontrivial BCs, in which the MFS will face a big challenge to select the right off-set distance. The logarithmic convergence for the HMM with increasing collocating points is much superior to the MFS which will result in an ill-conditioned and unstable system if collocating points are too large or the source locations are inappropriate. Therefore it is recommended that the HMM should be combined with MFS to solve large scale engineering problems with complicated geometry and BCs by using the HMM first and then tuning the optimal off-set distance from the boundary through the known HMM solutions as shown in present study.

Acknowledgement: The National Science Council of Taiwan is gratefully acknowledged for providing financial support under the grant no. NSC 95-2221-E-002-406 to carry out the present research, it is greatly appreciated.

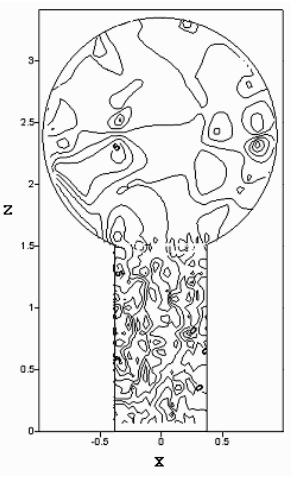

RMSE: 2
(a) MFS(d=2)

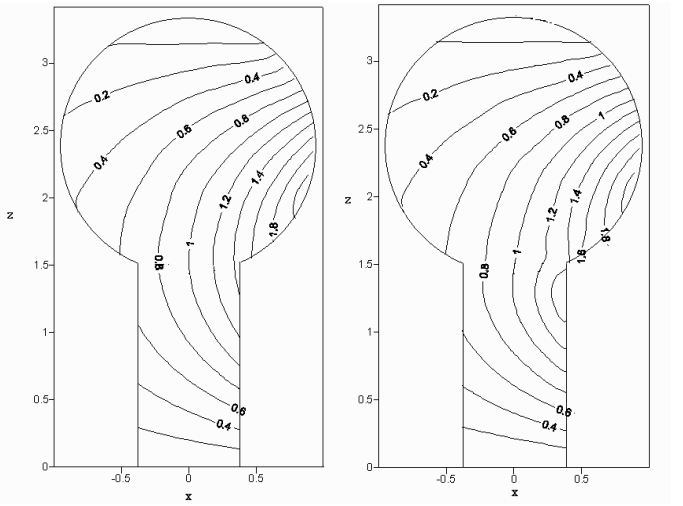

RMSE: 1.34E-4
(b) MFS (d=1.2)

RMSE: 4.11E-2
(c) HMM

Figure 20: The field solutions at y=0 cross-section by using (a) MFS (d=2), (b) MFS (d=1.2) (c) HMM for case 6-1.

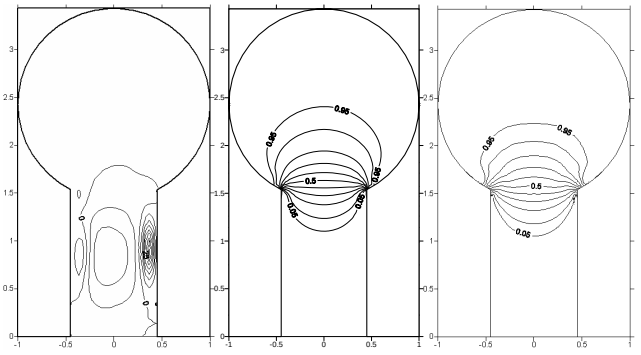

2261 nodes (a) MFS (d=1.2) 2310 nodes (b) LDQ 2261 nodes (c) HMM

Figure 21: The field solutions at z=0 cross-section by using (a) MFS (d=1.2) (b) LDQ (c) HMM for case 6-2.

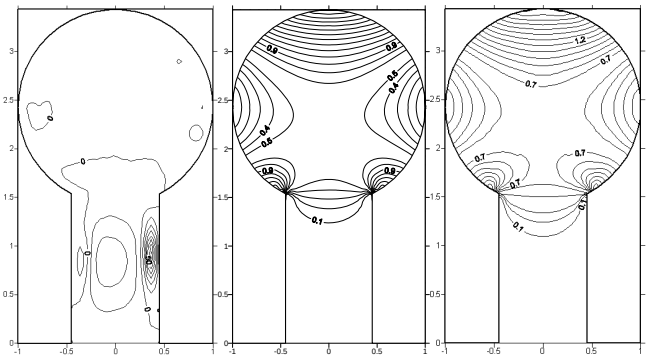

2261 nodes (a) MFS (d=1.2) 2310 nodes (b) LDQ 2261 nodes (c) HMM

Figure 22: The field solutions at z=0 cross-section by using (a) MFS (d=1.2) (b) LDQ (c) HMM for case 6-3.

Appendix A: The detail derivations of equations (14) and (15)

The null-fields of the boundary integral equations (BIEs) based on the direct method are

$$0=\int_B \frac{\partial \Phi^{(i)}(s,x^i)}{\partial n_s}\phi(s)dB(s)-\int_B \Phi^{(i)}(s,x^i)\frac{\partial \phi(s)}{\partial n_s}dB(s),\ \ x^i\in D^e, \tag{A1}$$

$$0=\int_B \frac{\partial^2 \Phi^{(i)}(s,x^i)}{\partial n_s \partial n_{x^i}}\phi(s)dB(s)-\int_B \frac{\partial \Phi^{(i)}(s,x^i)}{\partial n_{x^i}}\frac{\partial \phi(s)}{\partial n_s}dB(s),\ \ x^i\in D^e, \tag{A2}$$

where the superscript (i) denotes the interior domain, Φ is the single layer potential, and is equal to $1/(\bar{r}_{ij})$ for 3D Laplace equation. Let $\frac{\partial \Phi^{(i)}(s,x^i)}{\partial n_s}=A^{(i)}(s,x^i)$, and $\frac{\partial^2 \Phi^{(i)}(s,x^i)}{\partial n_s \partial n_{x^i}}=B^{(i)}(s,x^i)$. By employing the simple test method ($\partial\phi(s)/\partial n_s=0$ when $\phi(s)=1$), we can write Equations (A1) and (A2) respectively as follows:

$$\int_B A^{(i)}(s,x^i)dB(s)=0\ ,\ x^i\in D^e, \tag{A3}$$

$$\int_B B^{(i)}(s,x^i)dB(s)=0\ ,\ x^i\in D^e. \tag{A4}$$

When the field point x^i approaches the boundary, we can discretize Equations (A3) and (A4) as follows:

$$\sum_{j=1}^{N} A^{(i)}(s^j,x^i)\ell^j=0,\ x^i\in B, \tag{A5}$$

$$\sum_{j=1}^{N} B^{(i)}(s^j,x^i)\ell^j=0,\ x^i\in B. \tag{A6}$$

where ℓ^j is the half of distance of the $(j-1)-th$ source point and the $(j+1)-th$ source point. When the distribution of nodes is uniform, we are able to reduce Equations (A5) and (A6) to the following:

$$\sum_{j=1}^{N} A^{(i)}(s^j,x^i)=0,\ x^i\in B, \tag{A7}$$

$$\sum_{j=1}^{N} B^{(i)}(s^j,x^i)=0,\ x^i\in B, \tag{A8}$$

where

$$A^{(i)}\left(s^j,x^i\right)=-\frac{y_k n_k}{\bar{r}_{ij}^3} \tag{A9}$$

$$B^{(i)}\left(s^j,x^i\right)=\frac{n_k\overline{n_k}\overline{r_{ij}^2}-3y_ky_ln_k\overline{n_l}}{\overline{r_{ij}^5}} \tag{A10}$$

where $\bar{r}_{ij}=\left|s^j-x^i\right|$, n_k is the kth component of the outward normal vector at s^j; $\bar{n}_k$ is the kth component of the outward normal vector at x^i and $y_k=x_k^i-s_k^j$. The Equations (A7) and (A8) are the equations (14) and (15) in the text of Section 3; and Equations (A9) and (A10) are the Equations (10) and (11) in the text of Section 2.

Appendix B

Analytical derivation of diagonal coefficients of influence matrices for a spherical domain in 3D Laplace equation by separable kernels

By adopting the addition theorem (Abramowitz and Stegun 1972), we expand the two kernels in Eqs. (10) and (11) for interior problems as well as similarly for the exterior problems into separable kernels which separate the field point, x^i, and source point, s^j, as follows:

$$\bar{A}(s^j,x^i)=\frac{\partial\left(\frac{1}{r_{i,j}}\right)}{\partial\, r}=$$
$$\begin{cases}\bar{A}^{(i)}(s^j,x^i)=\\ \frac{1}{r^2}+\sum\limits_{n=1}^{\infty}\sum\limits_{m=0}^{n}(n+1)\frac{(n-m)!}{(n+m)!}\cos\left[m(\varphi-\theta)\right]P_n^m(\cos\eta)P_n^m(\cos\bar{\eta})\frac{r^n}{\rho^{n+2}}\\ \bar{A}^{(e)}(s^j,x^i)=\\ -\sum\limits_{n=1}^{\infty}\sum\limits_{m=0}^{n}n\frac{(n-m)!}{(n+m)!}\cos\left[m(\varphi-\theta)\right]P_n^m(\cos\eta)P_n^m(\cos\bar{\eta})\frac{r^{n-1}}{\rho^{n+1}}\end{cases} \tag{B1}$$

$$\bar{B}(s^j,x^i)=\frac{\partial\left(\frac{1}{r_{i,j}}\right)}{\partial\, r\,\partial\,\rho}=$$
$$\begin{cases}\bar{B}^{(i)}(s^j,x^i)=\\ -\sum\limits_{n=1}^{\infty}\sum\limits_{m=0}^{n}(n+1)(n+2)\frac{(n-m)!}{(n+m)!}\cos\left[m(\varphi-\theta)\right]P_n^m(\cos\eta)P_n^m(\cos\bar{\eta})\frac{r^n}{\rho^{n+3}}\\ \bar{B}^{(e)}(s^j,x^i)=\\ \sum\limits_{n=1}^{\infty}\sum\limits_{m=0}^{n}n(n+1)\frac{(n-m)!}{(n+m)!}\cos\left[m(\varphi-\theta)\right]P_n^m(\cos\eta)P_n^m(\cos\bar{\eta})\frac{r^{n-1}}{\rho^{n+2}}\end{cases} \tag{B2}$$

where $P_n^m(\bullet)$ is the associated Legendre polynomial, $s^j=(r,\theta,\bar{\eta})$ and $x^i=(\rho,\varphi,\eta)$ are defined in the spherical coordinates and plotted in Fig. 1(a) and 1(b). The superscripts (i) and (e) represent the interior and exterior problems respectively. For

simplicity we move the original coordinate system into a new coordinate system to take advantage of the concept of objective coordinate system of the RBFs. We then reformulate the Eqs. (B1) and (B2) to avoid dealing with the complex associate Legendre functions as follows:

$$A(s^j,x^i)=\begin{cases}A^{(i)}(s^j,x^i)=\sum\limits_{n=0}^{\infty}-(n+1)\frac{\rho^{n_l}}{r^{n_l+2}}\cos\left[n_l(\varphi-\theta)-\theta\right]\\ A^{(e)}(s^j,x^i)=\sum\limits_{n=0}^{\infty}n\frac{r^{n_l-1}}{\rho^{n_l+1}}\cos\left[n_l(\varphi-\theta)-\varphi\right]\end{cases} \tag{B3}$$

$$B(s^j,x^i)=\begin{cases}B^{(i)}(s^j,x^i)=\sum\limits_{n=0}^{\infty}-n(n+1)\frac{\rho^{n_l-1}}{r^{n_l+2}}\cos\left[n_l(\varphi-\theta)-\theta\right]\\ B^{(e)}(s^j,x^i)=\sum\limits_{n=0}^{\infty}-n(n+1)\frac{r^{n_l-1}}{\rho^{n_l+2}}\cos\left[n_l(\varphi-\theta)-\varphi\right]\end{cases}, \tag{B4}$$

where $n_l=\left(\frac{\rho}{a}\right)n$ and $l=0,\ 1,\ 2,\cdots n-1$ in which n is the quantity of source points we choose in the original coordinate system, n_l is the corresponding source points in the new coordinate system and a is the amplitude of the considered geometry. Since the rotation symmetry is preserved for the spherical boundary, the influenced matrices with the elements are described as

$$K_{ij}=K(r,\theta_j,\rho,\varphi_i), \tag{B5}$$

Where the kernel function k_{ij} can be the interior or exterior problem, $\theta_j,\quad \varphi_i$ are the angles of source and collocation points, respectively. By superimposing N lumped strength along the boundary, we have the following influence matrices,

$$[K]=\begin{bmatrix}k_0 & k_1 & \cdots & k_{N-1}\\ k_{N-1} & k_0 & \cdots & k_{N-2}\\ \vdots & \vdots & \ddots & \vdots\\ k_1 & k_2 & \cdots & k_0\end{bmatrix}, \tag{B6}$$

Where the elements of the first row can be obtained by

$$k_j=k(r,\theta_j,\rho,0), \tag{B7}$$

in which $\varphi=0$ is assigned without loss of generality. The matrix [K] in Eq. (B6) is found to be a circulant since the rotational symmetry for the influence coefficients is considered. By introducing the following bases for the circulants, I, $(C_N)^1$, $(C_N)^2\ldots$, and $(C_N)^{N-1}$, we can expand [K] into

$$[K]=k_0I+k_1(C_N)^1+k_2(C_N)^2+\cdots+k_{N-1}(C_N)^{N-1}, \tag{B8}$$

where I is an unit matrix and

$$C_N = \begin{bmatrix} 0 & 1 & 0 & \cdots & 0 & 0 \\ 0 & 0 & 1 & \cdots & 0 & 0 \\ \vdots & \vdots & \vdots & \ddots & \vdots & \vdots \\ 1 & 0 & 0 & \cdots & 0 & 0 \end{bmatrix}_{N\times N} . \tag{B9}$$

Based on the circulant theory (Davis 1979), the eigenvalues for the influence matrix, [K], are found as follows:

$$\lambda_l = k_0 + k_1\tau_l + k_2(\tau_l)^2 + \cdots + k_{N-1}(\tau_l)^{N-1}, \quad l = 0,1,2,\cdots,N-1, \tag{B10}$$

where λ_l and τ_l are the eigenvalues for [K] and $[C_N]$, respectively. It is easily found that the eigenvalues τ_l for the circulant $[C_N]$ are the roots for $\tau^N = 1$ as shown below:

$$\tau_l = e^{i\frac{2\pi l}{N}}, \quad l = 0,1,2,\cdots,N-1. \tag{B11}$$

Substituting Eq. (B11) into Eq. (B10), we have

$$\lambda_l = \sum_{m=0}^{N-1} k_m \tau_l^m = \sum_{m=0}^{N-1} k_m e^{i\frac{2\pi ml}{N}}, \quad l = 0,1,2,\cdots,N-1. \tag{B12}$$

According to the definition for k_m in Eq. (B5), we obtain

$$k_m = k_{N-m}, \quad m = 0,1,2,\cdots,N-1. \tag{B13}$$

Substitution of Eq. (B13) into Eq. (B12) it yields

$$\lambda_l = \sum_{m=0}^{N-1} k_m \cos(\frac{2\pi ml}{N}), \quad l = 0,1,2,\cdots,N-1. \tag{B14}$$

By setting $\varphi = 0$ without loss of generality, the Riemann sum of infinite terms reduces to the following integral

$$\lambda_l = \frac{1}{\Delta\theta}\lim_{N\to\infty}\sum_{m=0}^{N-1} K(m\Delta\theta,0)\cos(ml\Delta\theta)\Delta\theta \approx \frac{N}{2\pi}\int_0^{2\pi}\cos(l\theta)K(\theta,0)d\theta, \tag{B15}$$

where $\Delta\theta = \frac{2\pi}{N}$.

Interior problem

By employing the separable kernel $A^{(i)} = \left(s^j, x^i\right)$ for interior problem ($r > \rho$) in Eq. (B1) and the orthogonal conditions, Eq. (B15) reduces to

$$v_l^{(i)} = \begin{cases} 0, & l = 0 \\ \frac{-N(N-1)}{r^2}, & l = 1,\, 2, \cdots,\, N-1 \end{cases} \tag{B16}$$

Similarly, we have

$$\delta_l^{(i)} = \begin{cases} 0, & l = 0,\, 1 \\ \frac{-N(N-1)}{r^3}, & l = 2, \cdots,\, N-1 \end{cases} \tag{B17}$$

where $v_l^{(i)}$ and $\delta_l^{(i)}$ are the eigenvalues of $\left[A^{(i)}\right]$ and $\left[B^{(i)}\right]$ matrices, respectively. By employing the invariant property for the influence matrices, the first invariant is the sum of all the eigenvalues. The diagonal coefficients for the two matrices for the interior problem are obtained by adding all the eigenvalues and can be shown below:

$$Na_{jj} = \sum_{m=0}^{N-1} v_m^{(i)},\ \text{(j no sum)} \tag{B18}$$

$$Nb_{jj} = \sum_{m=0}^{N-1} \delta_m^{(i)}. \tag{B19}$$

Hence, the diagonal elements are easily determined from the first invariant as follows:

$$a_{jj} = \frac{-(N-1)^2}{r^2} \approx \frac{-4\pi^2}{\left(\frac{2\pi r}{N}\right)^2}, \quad N \gg 1 \tag{B20}$$

$$b_{jj} = \frac{-(N-1)(N-2)}{r^3} \approx \frac{-8\pi^3}{\left(\frac{2\pi r}{N}\right)^3}, \quad N \gg 1 \tag{B21}$$

Exterior problem

By employing the separable kernel for interior problem ($r > \rho$) in Eq. (B1) and the orthogonal conditions, we have

$$v_l^{(e)} = \begin{cases} 0, & l = 0 \\ \frac{2N(N-1)}{r^2}, & l = 1,\, 2, \cdots,\, N-1 \end{cases} \tag{B22}$$

$$\delta_l^{(e)} = \begin{cases} 0, & l = 0 \\ \frac{-2N^2(N-1)}{r^3}, & l = 1,\, 2, \cdots,\, N-1 \end{cases} \tag{B23}$$

By the same way, the diagonal coefficients for the two matrices for the exterior problem are in the form of

$$N\bar{a}_{ii} = \sum_{l=0}^{N-1} v_l^{(e)} \tag{B24}$$

$$N\bar{b}_{ii} = \sum_{l=0}^{N-1} \delta_l^{(e)}. \tag{B25}$$

Similarly, the diagonal terms of the influence matrices for the exterior problem are shown as follows:

$$\bar{a}_{jj} = \frac{2(N-1)^2}{r^2} \approx \frac{8\pi^2}{\left(\frac{2\pi r}{N}\right)^2}, \quad N \gg 1 \tag{B26}$$

$$b_{jj} = \frac{-2N(N-1)^2}{r^3} \approx \frac{-16\pi^3}{\left(\frac{2\pi r}{N}\right)^3}, \quad N \gg 1 \tag{B27}$$

The properties of the influence matrices for interior and exterior problems are shown in Tab. 7.

References

Abramowitz, M.; Stegun, I. A. (1972): Handbook of mathematical functions with formulation, graphs and mathematical tables. *Dove,* New York, USA.

Alves, Carlos J. S.; Antunes, Pedro R. S. (2005): The method of fundamental solutions applied to the calculation of eigenfrequencies and eigenmodes of 2D simply connected shapes. *CMC: Computers, Materials, & Continua*, Vol. 2, No. 4, pp. 251-266.

Antonio, J.; Tadeu, A.; Godinho, L. (2007): Sound wave propagation modeling in a 3D absorbing acoustic dome using the method of fundamental solutions. *ICCES*, Vol. 3, No. 3, pp. 157-162.

Atluri, S. N. (2004): The meshless method (MLPG) for domain & BIE discretizations. *Tech Science Press,* 677 pp, Forsyth, GA, USA.

Chen, W.; Tanaka, M. (2002): A meshfree, integration-free and boundary-only RBF technique. *Comput Math Appl,* Vol. 43, pp. 379-391.

Chen, C.W.; Fan, C.M.; Young, D.L.; Murugesan, K.; Tsai, C.C. (2005): Eigananalysis for membranes with sringers using the methods of fundamental solutions and domain decomposition. *CMES: Computer Modeling in Engineering and Sciences*, Vol. 8, No. 1, pp. 29-44.

Table 7: The properties of the influence matrices for the 3D Laplace equation

Kernel function	$A^{(i)}\left(s^j,x^i\right)=-\frac{y_k n_k}{\bar{r}_{ij}^3}$		$B^{(i)}\left(s^j,x^i\right)=\frac{n_k\overline{n_k}\bar{r}_{ij}^2-3y_k y_l n_k\overline{n_l}}{\bar{r}_{ij}^5}$	
Eigenvalue λ_l	Exterior	Interior	Exterior	Interior
	$v_l^{(e)}=\begin{cases}0, & l=0\\ \frac{2N(N-1)}{r^2}, & l=1,2,\cdots,N-1\end{cases}$	$v_l^{(i)}=\begin{cases}0, & l=0\\ \frac{-N(N-1)}{r^2}, & l=1,2,\cdots,N-1\end{cases}$	$\delta_l^{(e)}=\begin{cases}0, & l=0\\ \frac{-2N^2(N-1)}{r^3}, & l=1,2,\cdots,N-1\end{cases}$	$\delta_l^{(i)}=\begin{cases}0, & l=0,1\\ \frac{-N(N-1)}{r^3}, & l=2,\cdots,N-1\end{cases}$
Diagonal value	Analytical solution: $\frac{1}{N}\sum_{m=0}^{N-1}\lambda_m=\frac{Sum\ of\ diagonal\ terms}{N}$ (spherical domain only)			
	$\bar{a}_{jj}=\frac{2(N-1)^2}{r^2}\approx\frac{8\pi^2}{\left(\frac{2\pi r}{N}\right)^2}, \quad N>>1$	$a_{jj}=\frac{-(N-1)^2}{r^2}\approx\frac{-4\pi^2}{\left(\frac{2\pi r}{N}\right)^2}, \quad N>>1$	$b_{jj}=\frac{-2N(N-1)^2}{r^3}\approx\frac{-16\pi^3}{\left(\frac{2\pi r}{N}\right)^3}, \quad N>>1$	$b_{jj}=\frac{-(N-1)(N-2)}{r^3}\approx\frac{-8\pi^3}{\left(\frac{2\pi r}{N}\right)^3}, \quad N>>1$
	Numerical solution (arbitrary domain)			
	$\sum_{k=1}^{N}a_{i,k}-a_{i,i}$	$\sum_{k=1}^{N}a_{i,k}-a_{i,i}$	$-(\sum_{k=1}^{N}b_{i,k}-b_{i,i})$	$-(\sum_{k=1}^{N}b_{i,k}-b_{i,i})$

where $\bar{r}_{ij}=\left|x^i-s^j\right|$, $y_k=x_k^i-s_k^j$, $\bar{n}_k$ denotes the kth components of outward normal vector on x^i, respectively.

Chen, J. T.; Chang, M. H.; Chen, K. H. (2002a): Boundary collocation method for acoustic eigenanalysis of three-dimensional cavities using radial basis function. *Comput Mech,* Vol. 29, pp. 392-408.

Chen, J. T.; Chang, M. H.; Chen, K. H.; Lin, S. R. (2002b): The boundary collocation method with meshless concept for acoustic eigenanalysis of two-dimensional cavities using radial basis function. *J Sound Vib,* Vol. 257, pp. 667-711.

Chen, J. T.; Chen, I. L.; Wu, C. S. (2007): On the equivalence of MFS and Trefftz method for Laplace problems. *Computers & Math with Applic,* Vol. 53, pp. 851-879.

Chen, K. H.; Kao, J. H.; Chen, J. T.; Young, D. L.; Lu, M. C. (2006): Regularized meshless method for multiply-connected-domain Laplace problem. *Eng Anal Bound Elem,* Vol. 30, pp. 882-896.

Cheng, A. H. D.; Young, D. L.; Tsai, C. C. (2000): The solution of Poisson's equation by iterative DRBEM using compactly supported, positive definite radial basis function. *Engng Anal Bound Elem,* Vol. 24, pp. 549-557.

Davis, P.J. (1979): Circulant matrices. *John Wiley & Sons,* New York, USA.

Fairweather, G.; Karageorghis, A. (1998): The method of fundamental solutions for elliptic boundary value problems. *Adv Comput Math,* Vol. 9, pp. 69-95.

Godinho, L.; Tadeu, A.; Mendes, P. A. (2007): Wave propagation around thin structures using the MFS. *CMC: Computers, Materials, & Continua*, Vol. 5, No. 2, pp. 117-128.

Hon, Y.C.; Wei, T. (2005): The method of fundamental solution for solving multidimensional inverse heat conduction problems. *CMES: Computer Modeling in Engineering and Sciences*, Vol. 7, No. 2, pp. 119-132.

Hu, S.P.; Young, D.L.; Fan, C.M. (2008): FDMFS for diffusion equation with unsteady forcing function. *CMES: Computer Modeling in Engineering and Sciences*, Vol. 24, No. 1, pp. 1-20.

Hwang, W. S.; Hung, L. P.; Ko, C. H. (2002): Non-singular boundary integral formulations for plane interior potential problems. *Int J Numer Meth Eng,* Vol. 53, pp. 1751-1762.

Jin, B. (2004): A meshless method for the Laplace and biharmonic equations subjected to noisy boundary data. *CMES: Computer Modeling in Engineering and Sciences*, Vol. 6, No. 3, pp. 253-262.

Ling, L.; Takeuchi, T. (2008): Boundary control for inverse Cauchy problems of the Laplace equations. *CMES: Computer Modeling in Engineering and Sciences*, Vol. 29, No.1, pp. 45-54.

Liu, C.S. (2008): Improving the ill-conditioning of the method of fundamental solutions for 2D Laplace equation. *CMES: Computer Modeling in Engineering and Sciences*, Vol. 28, No. 2, pp. 77-94.

Ma, Q.W. (2007): Numerical generation of freak waves using MLPG_R and QALE-FEM methods. *CMES: Computer Modeling in Engineering and Sciences*, Vol. 18, No. 3, pp. 223-234.

Ma, Q.W. (2008): A new meshless interpolation scheme for MLPG_R method. *CMES: Computer Modeling in Engineering and Sciences*, Vol. 23, No. 2, pp. 75-90.

Marin, L. (2008): The method of fundamental solutions for inverse problems associated with the steady-state heat conduction in the presence of sources. *CMES: Computer Modeling in Engineering and Sciences*, Vol. 30, No. 2, pp. 99-122.

Pini, G.; Mazzia, A.; Sartoretto, F. (2008): Accurate MLPG solution of 3D potential problems. *CMES: Computer Modeling in Engineering and Sciences*, Vol. 36, No. 1, pp. 43-64.

Reutskiy, S. Y. (2004): The method of fundamental solutions for eigenproblems with Laplace and biharmonic operators. *CMC: Computers, Materials, & Continua*, Vol. 2, No. 3, pp. 177-188.

Reutskiy, S. Y. (2006): The method of external sources (MES) for eigenvalue problems with Helmholtz equation. *CMES: Computer Modeling in Engineering and Sciences*, Vol. 12, No. 1, pp. 27-40.

Shen, L. H.; Young D. L. (2007): Local differential quadrature method for elliptic equations in irregular domains. *PACON 2007*, Honolulu, Hawaii, pp. 135-151.

Shen, L. H.; Young D. L.; Lo, D.C.; Sun, C.P. (2009): Local differential quadrature method for 2-D flow and forced convection problems in irregular domains. *Numer Heat Transfer B*, Vol. 55, pp. 116-134.

Shiah, Y. C.; Tan, C. L.; Lee, V. G. (2008): Evaluation of explicit-form fundamental solutions for displacements and stresses in 3D anisotropic elastic solids. *CMES: Computer Modeling in Engineering and Sciences*, Vol. 34, No. 3, pp. 205-226.

Smyrlis, Y. S.; Karageorghis, A. (2001): Some aspects of the method of fundamental solutions for certain harmonic problems. *J Scientific Comput,* Vol. 16, pp. 341-371.

Tournour, M. A.; Atalla, N. (1999): Efficient evaluation of the acoustic radiation using multipole expansion. *Int J Numer Meth Eng,* Vol. 46, pp. 825-837.

Tsai, C. C. (2008): Particular solutions of Chebyshev polynomials for polyharmonic and poly-Helmholtz equations. *CMES: Computer Modeling in Engineering and Sciences*, Vol. 27, No. 3, pp. 151-162.

Tsai, C. C.; Young, D. L.; Cheng, A. H. D. (2002): Meshless BEM for three-dimensional Stokes flows. *CMES: Computer Modeling in Engineering and Sciences*, Vol. 3, No. 1, pp. 117-128.

Tsai, C.C.; Lin, Y.C.; Young, D.L.; Atluri, S.N. (2006): Investigations on the accuracy and condition number for the method of fundamental solutions. *CMES: Computer Modeling in Engineering and Sciences,* Vol.16, No. 2, pp. 103-114.

Tsangaris, T.; Smyrlis, S.; Karageorghis, A. (2004): A matrix decomposition MFS algorithm for biharmonic problems in annular domains. *CMC: Computers, Materials, & Continua*, Vol. 1, No. 3, pp. 245-258.

Vavourakis, V.; Sellountos, E. J.; Polyzos, D. (2006): A comparison study on different MLPG (LBIE) formulations. *CMES: Computer Modeling in Engineering and Sciences*, Vol. 13, No. 3, pp. 171-184.

Young, D. L.; Tsai, C. C.; Eldho, T. I.; Cheng, A. H. D. (2002): Solution of Stokes flow using an iterative DRBEM based on compactly-supported, positive definite radial basis function. *Comput Math Appl,* Vol. 43, pp. 607-619.

Young, D. L.; Chen, K. H.; Lee, C.W. (2005a): Novel meshless method for solving the potential problems with arbitrary domain. *J Comput Phys,* vol. 209, pp. 290-321.

Young, D. L.; Hwang, W. H.; Tsai, C. C.; Lu, H. L. (2005b): Accuracy of desingularized boundary integral equations for plane exterior potential problems. *Eng Anal Bound Elem,* Vol. 29, pp. 224-231.

Young, D.L.; Ruan, J.W. (2005): Methods of fundamental solutions for scattering problems of electromagnetic waves. *CMES: Computer Modeling in Engineering and Sciences*, Vol.7, No. 1, pp. 223-232.

Young, D.L.; Tsai, C.C.; Lin, Y.C. Chen, C.S. (2006a): The method of fundamental solutions for eigenfrequencies of plate vibrations. *CMC: Computers, Materials, & Continua*, Vol. 4, No. 1, pp. 1-10.

Young, D. L.; Chen, K. H.; Lee, C. W. (2006b): Singular meshless method using double layer potentials for exterior acoustics. *J Acoust Soc Am,* Vol. 119, pp. 96-107.

Young, D.L., Chen, K.H.; Chen, J.T.; Kao, J.H. (2007): A modified method of fundamental solutions with sources on the boundary for solving Laplace equations with circular and arbitrary domains. *CMES: Computer Modeling in Engineering and Sciences,* Vol.19, No, 3, pp. 197-221.

Zong, Z.; Lam, K.Y. (2002) A localized differential quadrature (LDQ) method and its application to the 2D wave equation. *Comput Mech*, Vol. 29, pp. 382–391.